Ion flux-film structure relationship during magnetron sputtering of WO

A. Hemberg, S. Konstantinidis, F. Renaux, J.P. Dauchot, R. Snyders

Ion flux–film structure relationship during magnetron sputtering of WO_3

A. Hemberg[1, 2], S. Konstantinidis[2], F. Renaux[1], J.P. Dauchot[2], and R. Snyders[1, 2]
[1] Materia Nova Research Center - Parc Initialis, 1, Avenue Copernic, B-7000 Mons, Belgium
[2] Chimie des Interactions Plasma- Surface, CIRMAP, Université de Mons - 20, Place du Parc, B-7000 Mons, Belgium

A. Hemberg : axel.hemberg@materianova.be, Fax : +32 65554941, tel: + 3265554945

S. Konstantinidis: stephanos.konstantinidis@umons.be, Fax : +3265554941, tel: +3265554956

F. Renaux : fabian.renaux@materianova.be , Fax : +32 65554941, tel: + 3265554952

J.P. Dauchot : jean-pierre.dauchot@umons.be , Fax : +32 65554941, tel: + 3265554943

R. Snyders : rony.snyders@umons.be , Fax : +32 65554941, tel: + 3265554955

Abstract

In this work, we have investigated the influence of the magnetic field configuration during magnetron sputtering of WO_3 in order to establish the ion flux–film structure relationship. An asymmetric bipolar pulsed DC magnetron sputtering (PDMS) was used with two magnetic field configurations: balanced (BM) and unbalanced (UMB) magnetic configurations. Ion Energy Distribution Functions (IEDF) of the main ion populations (Ar^+, O^+) were recorded. The IEDF are broad with, in addition of the thermalized distribution around 2 eV, two peaks with available ion kinetic energy up to 40-100 eV associated with the positive part of the pulse. Comparing the BM and UBM data, we calculated an increase by a factor of 5 of the ionic current while the average energy per ion was kept constant (~ 44 eV).

X-ray diffraction demonstrates the influence of the magnetic configuration on the coating phase constitution. The films are crystallized in the WO_3 monoclinic phase with preferential orientations along the c axis using the BM configuration and along the a axis using the UBM one's. On the other hand, it has been demonstrated that the grain size increases with the thickness using the BM configuration (up to 18 nm) while it remains constant using the UBM ones (~ 7 nm).

1. Introduction

Metal oxides like WO_3, SnO_2 and TiO_2 are widely used in gas sensors for air pollution monitoring systems, food industry, medical diagnosis equipment, and gas-leak-alarms. The sensor performances (sensitivity, selectivity, and ageing) are strongly dependent on the microstructural and crystallographic features of the active layer, namely the grain size, the density, the phase constitution, and the crystallographic face exposed to the gas [1-9]. Nowadays, most of these gas detection systems use thick (several µm) and porous layer of these materials as active part. Nevertheless, it is established that, if the layer thickness can be decreased to very low values (~100 nm), the interaction are limited to the film surface and the response time is significantly reduced [3]. Therefore, nowadays, a lot of efforts are developed to synthesize thin films of the aforementioned materials with tailored crystallographic properties (phase, texturation, grain size,…) in order to evaluate their potentiality in replacing the conventional thick active layers[4,5]. To synthesize these thin films, magnetron sputtering is one of the best candidates since it offers flexibility and easy up scaling. On the other hand, it has been demonstrated that the structure and properties of magnetron sputtered thin films can be modified by controlling the energy and flux of the ions impinging on the growing film surface [10].

By using balanced (BM) and unbalanced (UBM) magnetic configuration, it is possible to modify the ion bombardment during magnetron sputtering [11-17]. In an UBM, the outer ring of magnets is strengthened relative to the central pole. In this case, some magnetic field lines are directed towards the substrate and a fraction of the electrons generated in the magnetized plasma as well as some secondary electrons are no longer confined to the target region. The escaping energetic electrons spiral along the field lines and flow out towards the substrate undergoing ionizing collisions with gas atoms. As a consequence of ambipolar diffusion, ion and electron currents can be extracted without the need to externally bias the substrate and ions and electrons assist the deposition of the growing film. The current density collected on the substrate during unbalanced magnetron sputtering is usually one order of magnitude higher than that in conventional balanced magnetron sputtering.

Pulsed DC magnetron sputtering (PDMS) has been employed in a wide range of industrial research applications. PDMS processes operated in the frequency range 50-250 kHz with duty cycles varying from 0 to 40% allows the deposition of high quality transparent films in reactive atmospheres such as nitrogen or oxygen containing discharges. Pulsing the discharge leads to the elimination of accumulated charges on the insulating (oxide) films lowering on the target surface. Thus, arc formation on the target surface can be suppressed if an appropriate pulse frequency and duty cycle is chosen. Importantly, it has been shown that pulsing the magnetron leads to higher plasma densities and electron temperature adjacent to the substrate and therefore a the PDMS mode of operation allows ion energy fluxes to the growing film to be increased as compared to conventional DC discharge driven at the same power [18-22].

In this paper, we have studied the ion flux–film structure relationship during balanced and unbalanced pulsed DC magnetron sputtering of tungsten trioxide (WO_3).

2. Experimental setup

WO_3 films were prepared at 0.7 Pa in an Ar/O_2 gas mixture using a 10 cm in diameter tungsten target (99.9 %). The ratio of O_2 in the gas ($Ar + O_2$) mixture was kept constant to 83% in order to maintain the discharge in the so called oxidized regime. In these conditions, all films are fully stoichiometric as verified by X-Ray photoelectron spectroscopy (results not shown). The distance between target and substrate is set to 10 cm. Silicon (100) wafers were used as substrates, the substrate temperature during the deposition was 550°C. The coating thickness was varied from 50 to 400 nm. The cathode power is, for all experiments, set to 125 W. The schematic of the magnetron sputtering chamber is shown in **Fig 1**. The magnetic field architecture and the intensity of the magnetic field for the two different magnetron target configurations used in this study are shown in **Fig 2**. The magnetic field induction of the cathodes was measured using a portable gaussmeter, Metrolab THM 7025 Three Axis Transducer, with Hall probe. The field perpendicular and parallel to the target was measured in front of the target. The highest value of the parallel component of the magnetic induction is around 300 G for each geometry. The zero-field position is of 2 cm from the target surface in the UBM geometry. The intensity of the field component perpendicular to target the surface and at the center of the target is approximately 750 G for the BM and 400 G for the UBM geometries, respectively. An ENI RPG 5KW Asymmetric Bipolar Pulsed DC power supply working with a frequency of 50 kHz was used to generate the plasma. The pulse on time is of about 18 µs and the pulse reverse voltage off-time of about 2 µs. As an example, the target voltage and target current waveforms as measured with the UBM configuration are shown in **Fig 3**. The voltage initially increases up to - 1000 V, and stabilizes at -500 V after 5 µs, for the remaining pulse on time. In the pulse off time region, the voltage increases initially up to +400 V and then reduces to + 50 V.

A Hiden EQP 1000 mass spectrometer equipped with an energy analyzer was used to probe the plasma chemistry. The mass spectrometer extraction hood was placed at the substrate location. The mass spectrometer was electrically insulated keeping the extraction hood at the floating potential and therefore simulating a substrate left floating as it is the case during our deposition process. Ion energy distribution functions (IEDF) were acquired for Ar^+ and O^+ ions which are the main ion populations.

The crystallographic characterizations of the films were performed by X-Ray Diffraction (XRD) with a Siemens D5000 system in the Bragg-Brentano geometry using a monochromatized $Cu_{K\alpha}$ radiation. The measurements were realized with steps of 0.02° from 20 to 65°, at room temperature. The dwell time was set to 2 s. The crystalline phases were identified by comparison with spectra from the JCPDS database (01-083-0951). The WO_3 monoclinic phase (a= 7.301 Å, b= 7.539 Å, c= 7.689 Å, β =90.89) is described with the space group P21/n. The grain size (G) was evaluated through the Debye Scherrer method using the most intense peak of the diffractogram. When necessary, the diffraction peaks have been fitted by using a pseudo-Voigt function.

3. Results and discussions

Fig. 4 and **Fig. 5** show the Ar^+ and O^+ IEDF recorded for the BM and UBM configurations, respectively. Each IEDF exhibits a maximum at energy of about 2 eV corresponding to the kinetic energy gained by the ions as they travel through the sheath and accelerated by the potential difference between the plasma and the floating extraction hood. Therefore, this maximum corresponds to thermalized ions. In addition of this "thermalized peak", the IEDFs of both Ar^+ and O^+ reveal at least two additional contributions at much higher energy, namely around 40 eV and 75 eV. These additional peaks can be associated

with the phases B and C of the target voltage traces (see **Fig. 3**) which are related to the positive part of the pulse during which electrons are accelerated and the plasma potential is dramatically increased. Hence positive ions energy is increased as they travel through the sheath[23-24]. When comparing the BM and the UBM cases, one can observe that the IEDF profile are quite similar but that the IEDF intensities is increased in the case of the UBM configuration. In order to quantify the ion current in the different magnetic configurations, we calculated flux of ions current reaching the substrate (Γ_{ion}) by using the **Eq. 1** and the average ion energy ($<E_{ion}>$) by using the **Eq. 2**:

$$\Gamma_{ion} = \frac{\sum_{0}^{100} I(E)}{\sum_{0}^{100} I_{O^+(BM)}(E)} \qquad \text{(Eq. 1)}$$

$$\langle E_{ion} \rangle = \frac{\sum_{0}^{100} I(E).E}{\sum_{0}^{100} I(E)} \qquad \text{(Eq. 2)}$$

In (Eq. 1), the Γ_{ion} is normalized with respect to total flux of O^+ in BM.

The results of these calculations are reported in **Table 1**. The modification of the configuration of the magnetic field induces a strong variation in Γ_{ion} which increases by a factor of 5 for the UBM configuration when compared to the BM one. On the contrary, $<E_{ion}>$ is not affected, and $<E_{ion}>$ = 44 eV.

The **Fig. 6** shows the diffraction pattern of WO_3 films prepared at room temperature and at 550°C using BM and UBM configurations. It can be observe that without intentional heating of the growing film, the film is XRD amorphous. When heated to 550°C during deposition, WO_3 crystallizes in its monoclinic phase (JCPDS 01-083-0951) whatever the magnetic configuration employed. Nevertheless, when comparing the XRD patterns of the BM and UBM grown films, it appears that a different texturation of the material appears. For the BM configuration, a strong (002) texturation along the c axis is observed while for the

UBM configuration, a (200) texturation along the a axis is revealed. That behavior could be explained based on the thermodynamic stability of the mentioned crystallographic planes. Indeed, when enough energy is provided to the growing films, the (200) growth direction is favored because it corresponds to a larger atoms packing density and therefore to the growth direction producing the most stable material. This is consistent with our mass spectrometry data which highlight that for UBM, the ion current was increased by 5 times for the BM geometry, therefore allowing for a higher amount of energy to be supplied to the growing film.

Fig. 7 shows the evolution of the average grain size (G) as a function of the thickness for BM and UBM grown WO_3 thin films, respectively. Using the BM configuration (**Fig. 7**), it appears that G increases from 7 to 18 nm as the thickness increases from 25 to 400 nm which is consistent with reported data showing that, for a given depositing material/substrate combination and under a given set of deposition conditions, the grain size of the film increases as its thickness increases [27].

In the UBM configuration case, for which the thickness was varied between 50 to 400 nm, G is almost constant as a function of the film thickness. This result suggests that under these working conditions in which ion bombardment is intensified, the initial crystallites are not able to grow and to form larger grains even as the thickness (i.e. the deposition time) is increased. For comparison, for a 400 nm thick film G is ~ 18 nm for the BM configuration and ~ 6 nm for the UBM. In our study, the stress resulting from bombardment can be responsible for undervaluation of the G in both cases [25-26].

Based on these data, we have shown that it is possible to tailor both the texturation and the microstructure of reactively sputtered WO_3 thin films by varying the magnetic geometry of the magnetron.

4. Conclusions

In this work we have demonstrated, for WO_3 thin films synthesized by reactive magnetron sputtering, the key role of the magnetic field geometry (balanced, BM, and unbalanced, UBM) in the determination of the crystalline constitution and microstructure of the material. A clear correlation between the ion flux generated by the two types of magnetic field geometries and the thin films crystalline texturation and microstructure has been demonstrated.

By using energy resolved glow discharge mass spectrometry, we have shown that, in the UBM case, the ionic current (Ar^+ and O^+ ions) towards the growing film increases by a factor of 5 while the mean ion energy remains similar when compared to the BM situation. This stronger ionic bombardments leads to a clear (200) preferential orientation while the (0 02) orientation appears for the films prepared using the BM magnetron. This observation is understood based on the higher density, and therefore higher stability, of the WO_3 grain grown along the a axis (200). On the other hand, using the UBM configuration, the grain size remains constant when the films thickness increases from 50 to 400 nm (about 7 nm) while it evolves linearly from 7 nm to 20 nm in the BM case. This behavior has been again attributed to the strong bombardment in the UMB configuration which could limit the crystallite growth.

We believe that these data could be helpful for the design of WO_3-based sensitive coatings used in gas detection applications.

5. Acknowledgments

This work was supported by the department of the research programs of the DGO6 within the framework of program FIRST DOCA under the name of SENSCOAT project. The authors would like to thanks the financial supports of the Belgian Government to the IAP program (P06/08) and of the Walloon Region (DGO6) through the Opti2mat program. S. Konstantinidis is postdoctoral researcher of the Belgian National Fund for Scientific Research (FNRS).

6. References

Journals

1. J.J. Olaya, S.E. Rodil, S. Muhl, E. Sanchez, Thin Solid Films **474** (2005) 119-126

2. Baoshun Liu, Qi Hu Liping Wen , Xiujian Zhao , Thin Solid Films **517** (2009) 6569-6575

3. G. Korotcenkov, Sensors and Actuators B **107** (2005) 209-232

4. Scott C.Moulzolf et al, Sensors and Actuators B **77** (2001) 375-382

5. J.F. Chang et al., Sensors and Actuators B **84** (2002) 258-264

6. Won-Taek Moon, Kyu-Sung Lee, Youn-Ki Jun, Hyun-Su Kim, Seong-Hyeon Hong, Sensors and Actuators B **115** (2006) 123-127

7. M. Gillet, K. Aguir, M. Bendahan, P. Mennini, Thin Solid Films **484**, (2005) 358-363

8. Viacheslav Khatko, Stella Vallejos, Josep Calderer, Eduard Llobet, Xavier Vilanova, Xavier Correig, Sensors and Actuators B **126**, (2007) 400-405

9. L. J. LeGore, R.J. Lad, S.C. Moulzolf, J.F. Vetelino, B.G. Frederick, E.A. Kenike, Thin Solid Films **406** (2002) 79-86

10. I. Petrov, P.B. Barna, L. Hultman, J. E. Greene, J. Vac. Sci. Technol. A **21**, Issue 5, Sep-Oct 2003, 117-128

11. I. Petrov, F. Adibi, J. E. Greene, W. Sproul, W. D. Münz, J. Vac. Sci. Technol. A **10**, Issue 5, September 1992, 3283-3287

12. P.J. Kelly, R.D. Arnell, Vacuum **56** (2000) 159-172

13. J.J. Olaya, S.E. Rodil, S. Muhl, Thin Solid Films **516** (2008) 8319-8326

14. S.E. Rodil, J.J. Olaya, S. Muhl, B. Bhushan, G. Wei, Surface and Coatings Technology **201** (2007) 6117-6121

15. Jun Zhou, Zhe Wu, and Zhanhe Liu, Journal of University of Science and Technology, **15**, 6, December 2008, Page 775.

16. M. Zlatanović, R. Beloševac, N. Popović, A. Kunosić, Surf. Coat. Technol. **90** (1997) 143-149

17. M. Zlatanović, R. Beloševac , N. Popović, A. Kunosić, Surf. Coat. Technol. **106** (1998) 150-155

18. M. Rubio-Roy, C. Corbella, J. Garcia-Céspedes, M.C. Polo, E. Pascual, J.L. Andújar, E. Bertran, Diamond & Related Materials **16** (2007) 1286-1290

19. Sreejith Karthikeyan, Arthur E. Hill, John S. Cowpe, Richard D. Pilkington, Vacuum **85** (2010) 634-638

20. Harish C. Barshilia, K.S. Rajam, Applied Surface Science **255** (2008) 2925-2931

21. Harish C. Barshilia, B. Deepthi, K.S. Rajam, Thin Solid Films **516** (2008) 4168-4174

22. J W Bradley, H Bäcker, Y Aranda-Gonzalvo, P J Kelly and R D Arnell, Plasma Sources Sci. Technol. **11** (2002) 165-174

23. M. Misina, J. W. Bradley, H. Backer, Y. Aranda-Gonzalvo, S. K. Karkari, D. Forder, Vacuum 68 (2003) 171-181

24. J.W. Bradley, H. Backer, Surf. Coat. Technol. 200 (2005) 616-619

25. L. Parfitt, M. Goldiner, J. W. Jones, G. S. Was, J. Appl. Phys. 1995, 77, 3029.

26. P. G. Sanders, A. B. Witney, J. R. Weertman, R. Z. Valiev, R. W. Ziegel, Mater. Sci. Eng. A204 (1995) 7-11

Books

27. Milton Ohring, Materials science of thin films (Deposition and structure), 2nd edn, Academic Press

Table

	Unbalanced		Balanced	
	Ar^+	O^+	Ar^+	O^+
Γ_{ion}	6.8	2,4	1,4	1
$<E_{ion}>$	43,0	42,3	44,4	42,4

Tab. 1. Total current of ions reaching the substrate (Γ_{ion}) and average ion energy $<E_{ion}>$ using the BM and UBM magnetic configurations

Figures captions

Fig 1. Schematic view of magnetron sputtering chamber equipped with an unbalanced magnetron sputtering target.

Fig 2. Magnetic architecture of the magnetron. (a) balanced magnetron (BM) and (b) unbalanced magnetron (UBM).

Fig 3. Target Voltage and current waveforms measured with an oscilloscope during PDMS discharge driven with a frequency of 50 kHz and a pulse off time of 1936 ns (UBM case).

Fig 4. IEDF of Ar^+ using the BM and UBM magnetic configurations.

Fig 5. IEDF of O^+ using the BM and UBM magnetic configurations.

Fig 6. XRD patterns of 100 nm thick WO_3 film synthesized (a) without intentional heating, (b) at 550°C using the BM configuration and (c) at 550°C using the UBM configuration.

Fig.7. Average grain size (G) as a function of the film thickness for films synthesized using the BM and the UBM configurations.

Fig 1.

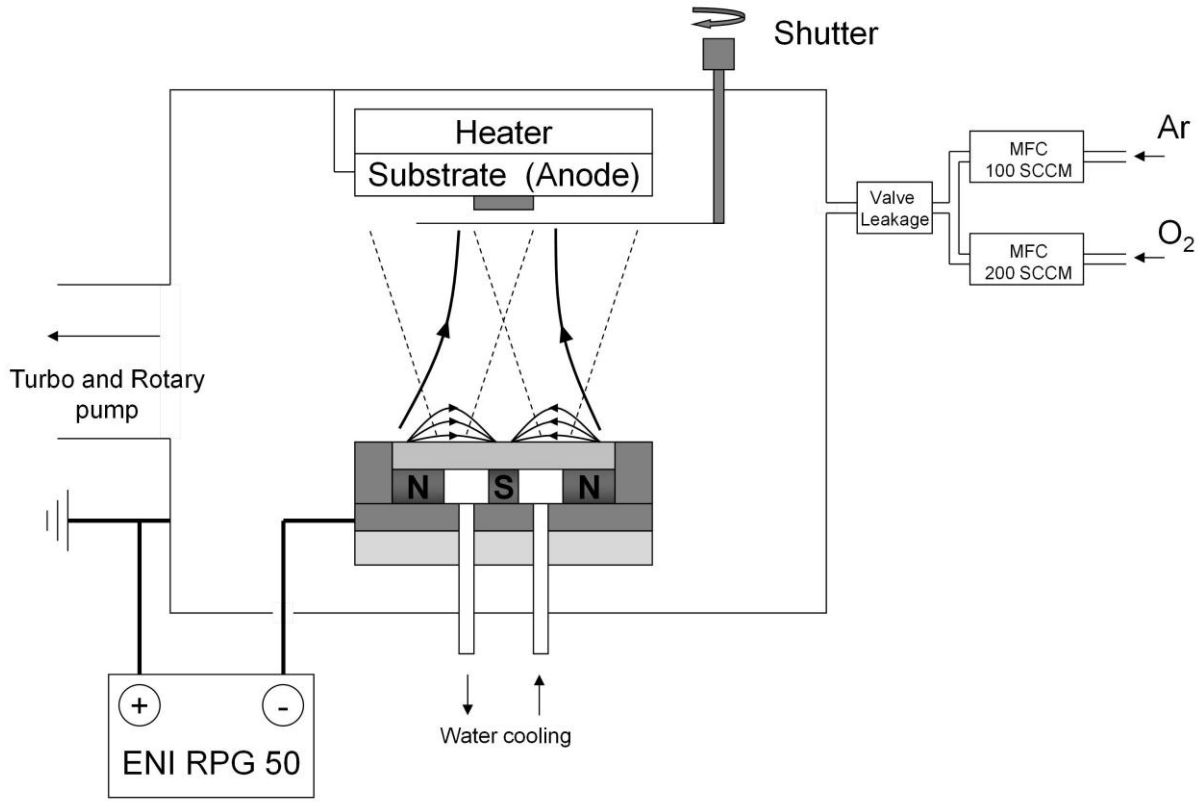
Shutter
Heater
Substrate (Anode)
Valve
Leakage
MFC
100 SCCM
MFC
200 SCCM
Ar
O2
Turbo and Rotary
pump
N
S
N
+
-
ENI RPG 50
Water cooling

Fig 2.

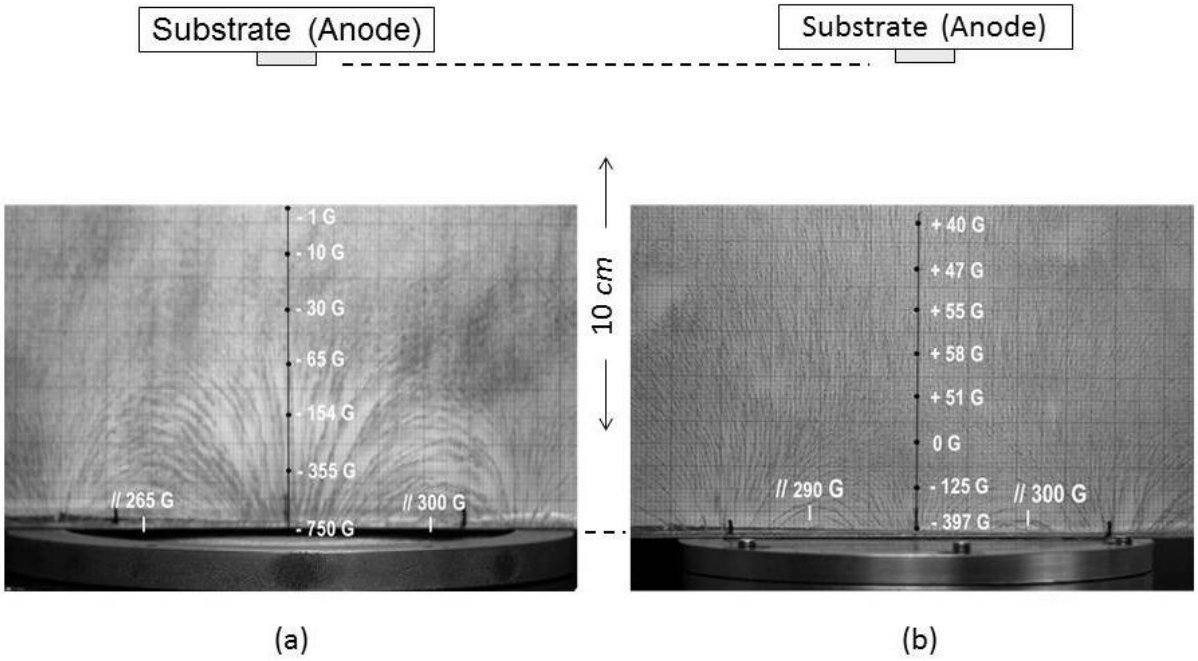
Substrate (Anode)
Substrate (Anode)
- 1 G
- 10 G
- 30 G
- 65 G
- 154 G
- 355 G
// 265 G
// 300 G
- 750 G
10 cm
+ 40 G
+ 47 G
+ 55 G
+ 58 G
+ 51 G
0 G
// 290 G
- 125 G
// 300 G
- 397 G
(a)
(b)

Fig 3.

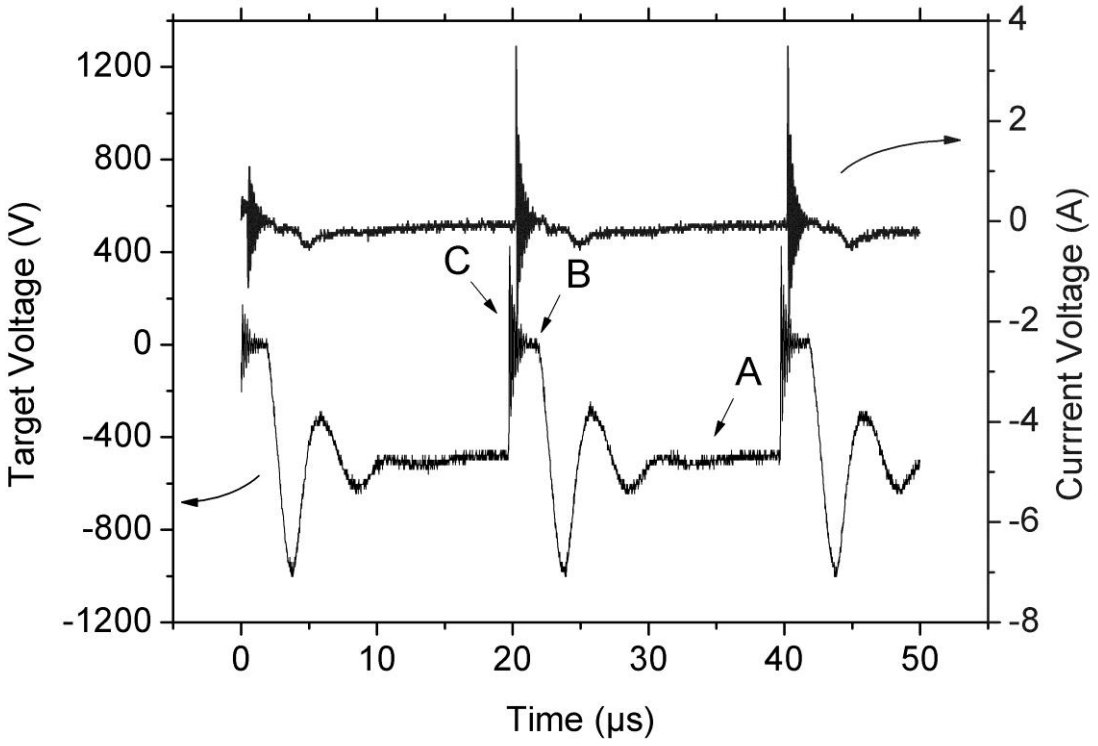
Target Voltage (V)
Currrent Voltage (A)
Time (μs)
1200
800
400
0
-400
-800
-1200
4
2
0
-2
-4
-6
-8
0
10
20
30
40
50
A
B
C

Fig 4.

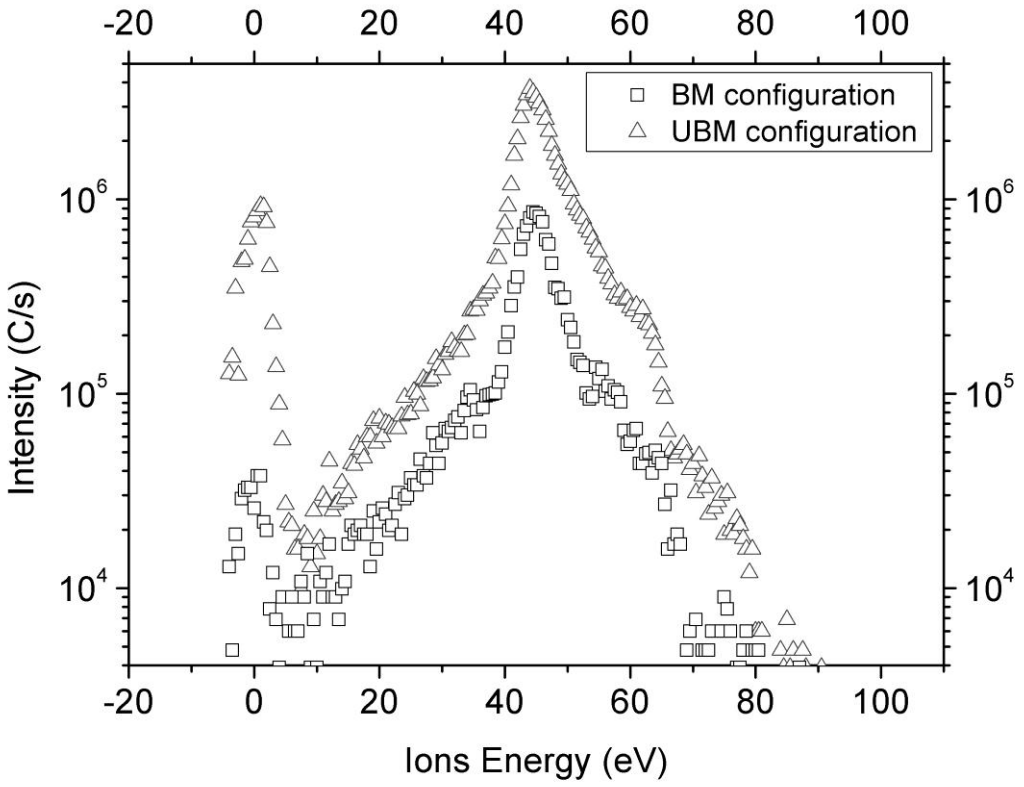
BM configuration
UBM configuration
Intensity (C/s)
Ions Energy (eV)
-20
0
20
40
60
80
100
10^4
10^5
10^6

Fig 5.

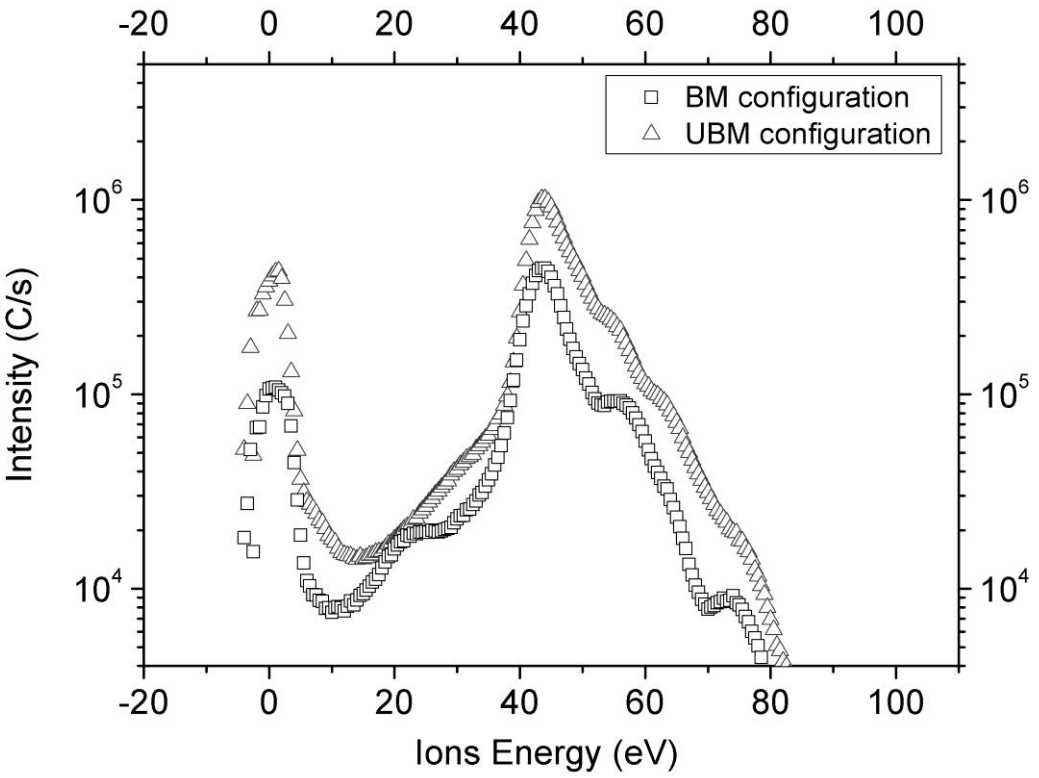
BM configuration
UBM configuration
Intensity (C/s)
Ions Energy (eV)
-20
0
20
40
60
80
100
10^4
10^5
10^6

Fig 6.

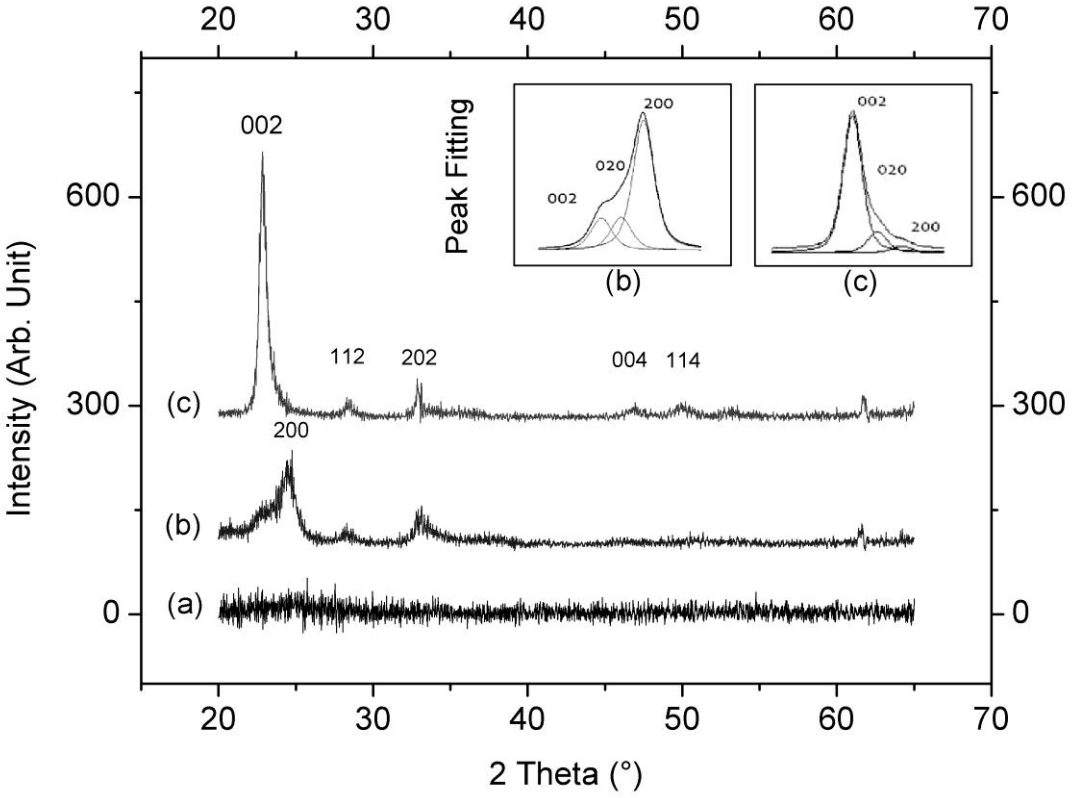
20
30
40
50
60
70
600
300
0
Intensity (Arb. Unit)
2 Theta (°)
002
112
202
004
114
200
(a)
(b)
(c)
Peak Fitting
200
020
002
(b)
002
020
200
(c)

Fig 7.

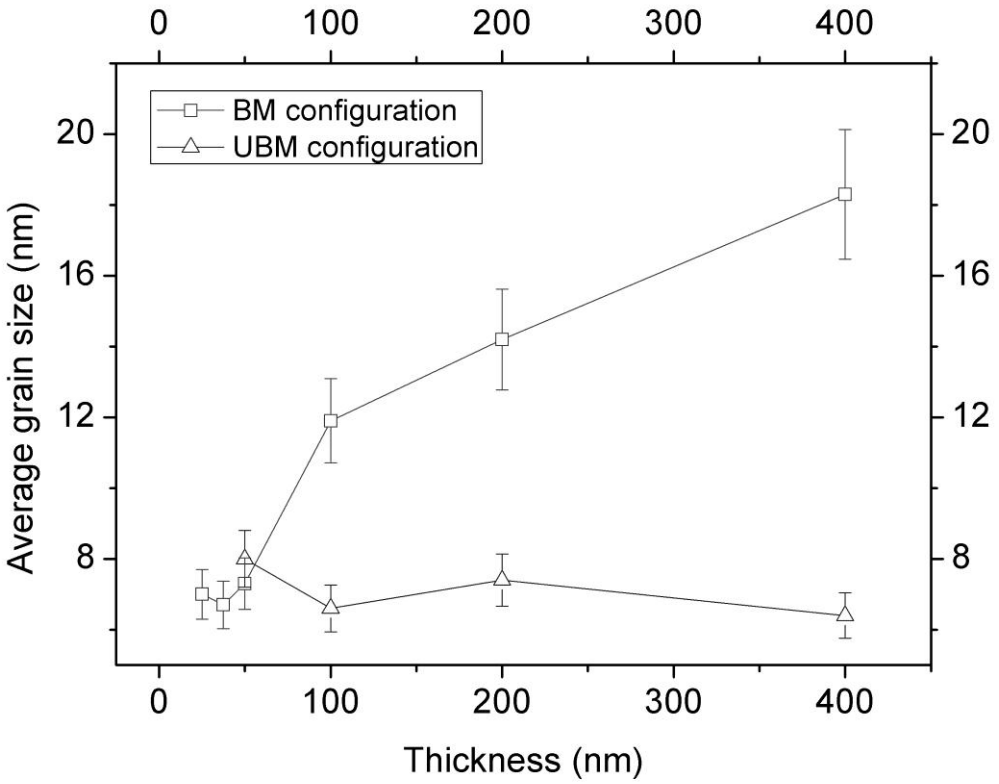
BM configuration
UBM configuration
Average grain size (nm)
Thickness (nm)
0
100
200
300
400
8
12
16
20